# Processes Driving Subseasonal Variations of Upper Ocean Heat Content in the Equatorial Indian Ocean

Ashneel Chandra[1,2] , Noel Keenlyside[1,2,3] , Lea Svendsen[1,2] , and Awnesh Singh[4]

[1]Geophysical Institute, University of Bergen, Bergen, Norway, [2]Bjerknes Centre for Climate Research, Bergen, Norway, [3]Nansen Environmental and Remote Sensing Center, Bergen, Norway, [4]The University of the South Pacific, Suva, Fiji

**Abstract** In the equatorial Indian Ocean, the largest subseasonal temperature variations in the upper ocean are observed below the mixed layer. Subsurface processes can influence mixed layer temperature and consequently air-sea coupling. However, the physical processes driving temperature variability at these depths are not well quantified. During the boreal winter, the Madden–Julian Oscillation (MJO) partly drives upper ocean heat content (OHC) variations. Therefore, to understand processes driving subseasonal OHC variability in the equatorial Indian Ocean, we use an observationally constrained, physically consistent ocean state estimate from the *Estimating the Circulation and Climate of the Ocean* (ECCO) Consortium. Using a heat budget analysis, we show that the main driver of subseasonal OHC variability in the ECCO ocean state estimate is horizontal advection. Along the equator, OHC variations are driven by zonal advection while the role of meridional advection becomes more important away from the equator. During the active phase of the MJO, net air-sea heat fluxes damp OHC variability along the equator, while away from the equator net air-sea heat fluxes partly drive OHC variability. Equatorial OHC variations are found to be associated with processes driven by Kelvin and Rossby waves consistent with previous studies. By quantifying the physical processes, we highlight the important role of ocean dynamics in contributing to the observed variations of subseasonal OHC in the equatorial Indian Ocean.

**Plain Language Summary** Heat stored in the upper ocean can have important implications for the interaction between the ocean and the atmosphere. The tropical Indian Ocean is unique in that it is where one of the strongest sources of large-scale atmospheric convection known as the Madden-Julian Oscillation (MJO) typically originates on timescales ranging from 1 to 3 months. The MJO moves eastward exerting stresses on the ocean surface that generates planetary-scale waves. The waves generated on these timescales largely propagate eastward along the equator and westward slightly off the equator. In this study, we investigate the MJO's impact on the upper Ocean Heat Content (OHC) and the different mechanisms causing it to vary. In the upper 200 m of the ocean, ocean currents and temperature contrasts in the east-west direction are important in driving changes of OHC along the equator while slightly off the equator, ocean currents and temperature contrasts in the north-south direction become more important. Ocean temperature anomalies are also found to be produced by the MJO forced waves. The ocean heat content anomalies move eastward along the equator and westward slightly off the equator and have the strongest signal at depths of between 50–150 m.

## 1. Introduction

The largest subseasonal to seasonal (S2S) upper ocean temperature variability in the equatorial Indian Ocean is observed below the mixed layer between depths of 50–150 m for example, (Konda et al., 2023). The Madden–Julian Oscillation (MJO) partly drives upper ocean temperature variability during the boreal winter through the forcing of equatorial waves (e.g., Boulanger & Menkes, 1995; Cane & Moore, 1981; Cane & Sarachik, 1977; DeMott et al., 2015; Hendon et al., 1998; Matthews et al., 2010; Pujiana & McPhaden, 2020). Subseasonal mixed layer temperature (MLT) dynamics are well understood (e.g., Chi et al., 2014; Drushka et al., 2012; Halkides et al., 2015; McPhaden & Foltz, 2013). However, the physical processes driving temperature subseasonal variability below the mixed layer, where the largest variations in temperature and ocean heat content (OHC) occur, are not well quantified. Therefore, in this study, we investigate the OHC variability in the upper 200 m, which captures the largest observed subseasonal temperature variations. We go further to quantify the physical processes that cause the observed patterns of OHC variability associated with the MJO. This is achieved using an ocean state estimate that is now capable of resolving processes that occur on subseasonal timescales.

**Writing – review & editing:**
Ashneel Chandra, Noel Keenlyside,
Lea Svendsen, Awnesh Singh

Studies of subseasonal MLT processes have identified surface heat fluxes (Drushka et al., 2012), ocean dynamics (Halkides et al., 2015; McPhaden & Foltz, 2013), and subsurface vertical processes (Chi et al., 2014; Halkides et al., 2015; McPhaden & Foltz, 2013) as drivers of MLT variability in the equatorial Indian Ocean. These studies have shown that, in addition to surface heat fluxes, subsurface processes can drive MLT variability and consequently be important for air-sea coupling. However, observational studies using Argo have large uncertainties due to the inhomogeneous spatiotemporal distribution of the Argo floats. Mooring based studies are usually limited to the investigation of specific observed events.

The upper OHC is hypothesized to have a delayed feedback on the MJO via oceanic equatorial waves. Webber et al. (2010) and Rydbeck et al. (2021) describe one mechanism by which the interaction between OHC and the MJO occurs. Momentum forcing from the westerly wind stress associated with Intraseasonal Oscillations (ISOs) such as the MJO forces eastward propagating downwelling Kelvin waves. The Kelvin waves are associated with the eastward advection of warm OHC anomalies. The Kelvin waves and the associated warm OHC anomalies reflect off the coast of Sumatra as downwelling Rossby waves and propagate westward. Upon reaching the central part of the Indian Ocean basin, the warm OHC anomalies associated with the Rossby waves can contribute to a warming sea surface temperature (SST) response in the central and western Indian Ocean. The SST gradients associated with this Rossby wave modulation of OHC can contribute to boundary layer convergence, which can trigger atmospheric convection, potentially affecting MJO intensity, triggering an MJO event, or modifying the low-frequency tail of MJO variability (Rydbeck et al., 2017; Webber et al., 2012). Further support for the interaction between OHC and the MJO is provided by the relationship shown by Moum et al. (2016), in which weaker MJO events are followed by stronger MJO events and vice versa, depending on the available OHC. Recently, Rydbeck et al. (2023) have shown that OHC is a reservoir of column integrated moist static energy (MSE) for the MJO. Therefore, given the importance of OHC in influencing air-sea interactions on subseasonal timescales and consequently the MJO, it is important to understand the various physical processes that contribute to driving the observed changes in OHC.

Advances in constraining models with observations have given us a new opportunity to understand physical processes with ocean state estimates (Wunsch & Heimbach, 2013). Constrained by observations in a dynamically and kinematically consistent way, ocean state estimates are a useful tool to provide a mechanistic understanding that would otherwise not be possible with observations, models, or ocean reanalysis constrained by data assimilation. The ECCO (Estimating the Circulation and Climate of the Ocean) Consortium has released a new version of its ocean state estimate, ECCO Version 4 Release 4 (ECCOv4r4). Unlike previous releases, which only provided monthly model fields, ECCOv4r4 now provides daily model fields, allowing the study of higher-frequency processes. Therefore, the goal of the current study is to use ECCOv4r4 to gain new insights into the physical processes driving subseasonal OHC variability. Using this new product, we aim to address the following research questions: (a) Quantifying the contributions of the physical processes driving the subseasonal upper OHC variability in the equatorial Indian Ocean, and (b) Identify the dominant physical processes driving the observed patterns of OHC variability associated with the MJO.

## 2. Data and Methods

### 2.1. ECCOv4r4

We use the daily model fields from Estimating the Circulation and Climate of the Ocean Version 4 Release 4 (ECCOv4r4) (ECCO Consortium, 2021; Forget et al., 2015; Wang & Fenty, 2021; Wunsch & Heimbach, 2013) to investigate the physical processes driving S2S OHC variations. ECCOv4r4 is an optimal solution of the Massachusetts Institute of Technology general circulation model (MITgcm) (Marshall et al., 1997). The ECCOv4 configuration of MITgcm solves the primitive equations for the case of a Boussinesq, hydrostatic ocean and uses a nonlinear free surface with real freshwater exchanges. While observations (e.g., altimetry, Argo floats, XBTs, CTDs, marine mammals, gliders and moorings) are used to constrain the model solutions in a least squares sense, the ECCO state estimate retains physical consistency via the adjoint method (Heimbach et al., 2005) to produce a coherent and physically consistent description of the ocean's time-evolving state. One limitation of the least squares fit used to constrain the model solutions is that nonlinear relationships between observations and model solutions may not be accurately represented.

We chose to use the ECCO ocean state estimate for this study as the physical consistency of the model solutions of this product satisfies the conservation laws of the model (while being constrained by observations), so that no

nonphysical sources and sinks are introduced in the state estimate fields. This is in contrast to traditional data assimilation techniques where constraining the model with observations inadvertently leads to analysis increments introduced to the model fields by processes not governed by model physics. The dynamical and kinematical consistency of the ECCO state estimate allows property budgets of heat, salt and volume to be closed while being constrained by observations so that a realistic and complete understanding of the physical processes within the model framework is possible.

ECCOv4r4 employs the LLC90 (Lat-Lon-Cap 90) grid in the native configuration. The horizontal grid has an average resolution of 1°, which is approximately 110 km near the equator. The vertical grid has 50 levels with thickness ranging from 10 m near the surface to 457 m near the ocean bottom. The course horizontal and vertical grid resolution limits the ability of the state estimate fields to resolve eddies and to accurately resolve mixed layer processes, which can have upscale effects on subseasonal mixed layer temperature budgets for example, (Shinoda, 2005; Shinoda et al., 2013). In addition, the parametrizations required due to unresolved processes resulting from the course grid have limitations and are not perfect. The atmospheric forcing of heat, momentum and water is from the European Centre for Medium-Range Weather Forecasts interim reanalysis (ERA-Interim) (Dee et al., 2011). The atmospheric forcings are adjusted with the added constraint that the adjustments are within the uncertainty of the ERA-Interim forcing variables so that the ECCO state estimate fields are consistent with observations. One consequence of this adjustment of the forcing fields and the fact that the ECCO estimates are derived from an ocean only general circulation model is that the ECCO estimates cannot be used to address the origin of atmospheric forcing (Buckley et al., 2014).

### 2.2. Observations

As a proxy for large-scale atmospheric convection associated with the MJO, we use Outgoing Longwave Radiation (OLR) data from the National Oceanic and Atmospheric Administration (NOAA) Physical Sciences Laboratory (PSL), Boulder, Colorado, USA, from their website at https://psl.noaa.gov (Liebmann & Smith, 1996). The NOAA Interpolated OLR data has daily temporal resolution and a 2.5° latitude × 2.5° longitude global spatial resolution. The MJO phase and amplitude are characterized by the Real-time Multivariate MJO series 1 and 2 (RMM1 and RMM2) indices. RMM1 and RMM2 are the first two leading principal components from a combined EOF analysis of lower and upper level zonal winds (u850 and u200) and OLR as described in Wheeler and Hendon (2004). The daily RMM indices are acquired from the Australian Bureau of Meteorology from their website at http://www.bom.gov.au/climate/mjo/.

Satellite altimeter derived gridded sea level anomaly (SLA) data are obtained from the Copernicus Marine Data Store from their website at https://data.marine.copernicus.eu/product/SEALEVEL_GLO_PHY_L4_MY_008_047/description (CMEMS, 2023; Ducet et al., 2000; Pascual et al., 2006). The daily SLA fields are available on a regular ¼° × ¼° grid. The gridded data are produced using optimal interpolation to merge the L3 along-track measurement from different altimeter missions. The satellite altimeter derived SLA is compared with the model sea surface height anomaly corrected for the inverted barometer effect, Dynamic SSH (SSHDYN). NOAA ¼° Daily Optimum Interpolation Sea Surface Temperature (OISST) V2 data for comparison with the model Potential Temperature at 5 m depth, $\theta$ ($-5$ m), was provided by the NOAA PSL, Boulder, Colorado, USA, from their website at https://psl.noaa.gov (Huang et al., 2021; Reynolds et al., 2007).

The performance of ECCO is evaluated using mooring data from mid-September 2011 to mid-January 2012 from the DYNAMO field campaign. We use data from two mooring sites D1 and D2 located at 0°N, 78.9°E and 1.5°S, 78.8°E (red and blue stars in Figure 1a). The data is obtained from the DYNAMO Legacy Collection (Lien & Moum, 2019) hosted by UCAR/NCAR - Earth Observing Laboratory (https://data.eol.ucar.edu/dataset/347.230). While observations from moorings are used to constrain the ECCO ocean state estimate model fields, these specific moorings have not been used to constrain the solutions of MITgcm. Hence, data from these moorings form a good observational data set to validate and evaluate the performance of the ECCO model fields. We compare the daily averaged mooring temperature data with the ECCO temperature data at the nearest grid points (red and blue circles in Figure 1a). The ECCO daily averaged potential temperature and salinity are first used to obtain in situ temperature following the Thermodynamic Equation Of Seawater–2010 (TEOS–10) convention (IOC, 2010; McDougall & Barker, 2011) so that the same quantities are compared.

The ECCO temperature is in good agreement with the mooring temperature values in the upper 5 m with correlations of 0.89 at D1 and 0.92 at D2 as depicted in Figures 1f and 1g. The correlations are gradually reduced at
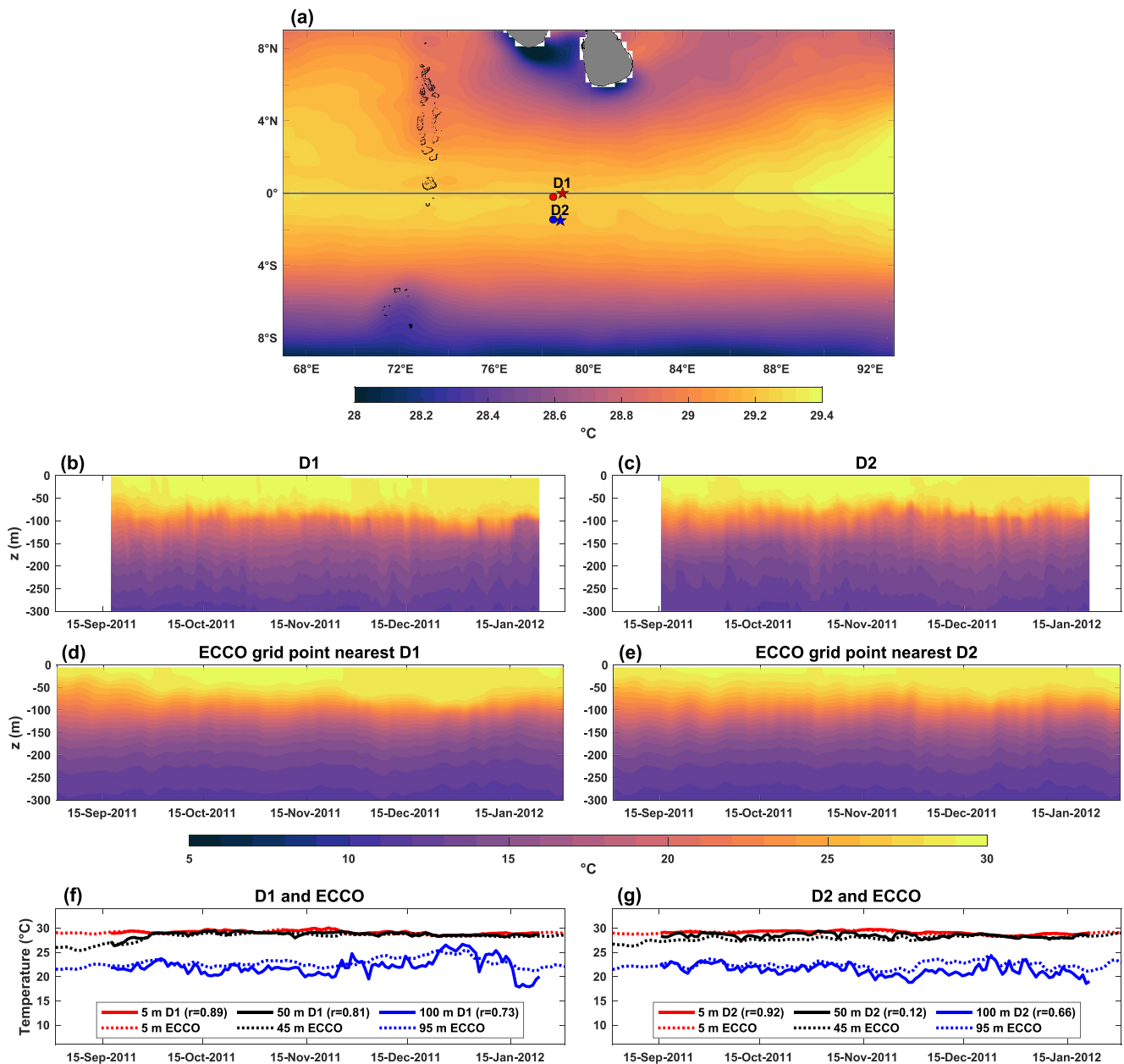
**Figure 1.** ECCO temperature data is compared with two moorings deployed during the DYNAMO field campaign from mid-September 2011 to mid-January 2012. The moorings D1 and D2 and their locations are shown in (a) where D1 (red star) is located at 0°N, 78.9°E and D2 (blue star) is located at 1.5°S, 78.8°E with the corresponding nearest ECCO grid points depicted as red and blue circles. The shading in (a) shows the mean sea surface temperature from NOAA OISST. Time-depth temperature from mooring D1 is shown in (b) while the corresponding nearest ECCO time-depth temperature at the location of the red circle is shown in (d). Time-depth temperature from mooring D2 is shown in (c) while the corresponding nearest ECCO time-depth temperature at the location of the blue circle is shown in (e). The time series of temperature from moorings D1 and D2 are shown in (f) and (g) respectively along with the corresponding ECCO temperature at selected depths of ∼5 m (red), ∼50 m (black) and ∼100 m (blue). The solid curves in (f) and (g) are mooring temperature values while the dashed curves are ECCO temperature values at approximately the same depth.

deeper levels, with the correlations at 100 m being 0.75 at D1 and 0.66 at D2. With the exception of the low correlation of 0.12 at 50 m depth for D2, there is good agreement between the mooring and ECCO temperature values. The mooring temperature has higher frequency variability, some of which is not well captured in ECCO, possibly because of the subgrid scale parametrizations and coarse resolution of the LLC90 grid used for MITgcm. This comparison with observations supports the usefulness of the ECCO data in our study.

## 2.3. Heat Budget

The upper ocean heat budget is analyzed to determine the contributions of the different physical processes driving OHC variability. We use the model specific formulation of the temperature tendency (Equation 4 in Forget et al. (2015)) to compute the heat budget. The physical interpretation of the budget terms is described by the following equation from Buckley et al. (2014):

$$\underbrace{\rho_o C_p \int_{-D}^{\eta} \frac{\partial \theta}{\partial t} dz}_{\text{OHCT}} = \underbrace{\rho_o C_p \int_{-D}^{\eta} -\nabla \cdot (\boldsymbol{u}\theta + \boldsymbol{u}^*\theta) dz}_{\text{ADV}} + \underbrace{\rho_o C_p \int_{-D}^{\eta} -\nabla \cdot \boldsymbol{K} dz}_{\text{DIF}} + \underbrace{Q_{\text{net}}}_{Q} \quad (1)$$

where $\rho_o$ is the mean seawater density (1,029 kg m$^{-3}$); $C_p$ is the heat capacity (3994 J kg$^{-1}$ K$^{-1}$); $\theta$ is the potential temperature; $\eta$ is the free surface; $D$ is the depth in meters; $\boldsymbol{u}$ is the three-dimensional (explicit model) velocity; $\boldsymbol{u}^*$ is the parameterized eddy-induced transport velocity; $\boldsymbol{K}$ is the diffusive temperature flux resulting from diapycnal diffusion and parameterized isopycnal diffusion; and $Q_{\text{net}}$ is the net (turbulent plus radiative) air-sea heat flux.

The left-hand side of Equation 1 represents the ocean heat content tendency (OHCT). The right-hand side shows the different physical processes contributing to changes in OHC. The first term on the right-hand side represents the three-dimensional ocean heat transport convergence, which for simplicity is called advection (ADV). The advection term is further decomposed into zonal (ADV$_x$), meridional (ADV$_y$) and vertical (ADV$_v$) components. The second term on the right-hand side is the diffusion (DIF) term. The diffusion term includes diapycnal and isopycnal components as well as turbulence in the mixed layer (Gaspar et al., 1990; Redi, 1982). The diffusion term is also decomposed into zonal (DIF$_x$), meridional (DIF$_y$) and vertical (DIF$_v$) components. The third term, $Q$ is the net air-sea heat flux, which includes latent heat flux, sensible heat flux, longwave radiation, and shortwave radiation. Shortwave radiation penetrates the upper 200 m of the water column decaying exponentially according to Jerlov Type IA-2 water (Paulson & Simpson, 1977).

The heat budget terms are evaluated on the ECCOv4r4 native grid (LLC90) using the appropriate diagnostic outputs from MITgcm, as described in Piecuch (2017). While ECCOv4r4 covers the period from 1992 to 2017, we only use the data from the ARGO period (2005–2017) as the state estimates are better constrained by observations.

The differences between the model horizontal grid orientation and the conventional zonal (east-west) and meridional (north-south) orientation are treated as follows. The horizontal advection term is computed from the model horizontal orientation components to ensure budget closure. Otherwise, we consider the conventional zonal and meridional advection components. Consequently, the sum of zonal and meridional advection is not always equal to the horizontal advection term. This does not affect our results greatly, as the model and conventional horizontal components are similar in the central equatorial Indian Ocean and only show major differences near the coastal boundaries.

We isolate subseasonal anomalies as follows: First, we remove the long-term mean (relative to the 2005–2017 period) and then remove the linear trend. Second, we remove the daily climatological seasonal cycle. Finally, the fields are bandpass filtered by applying a zero-phase Butterworth filter to obtain the 30–150 days timescale signal. A wide temporal band, relative to S2S timescales, is chosen to capture the slower response of the ocean to atmospheric forcing. After filtering the heat budget terms, we observe that a non-negligible residual is introduced near the end of the timeseries. The end of our analysis period also coincides with the end of the ocean state estimate period. Hence when we specifically analyze heat budget terms, we discard the final year to retain budget closure.

Unless otherwise stated, the OHC budget analysis is computed for the upper 200 m of the ocean. The vertical integration is performed by multiplying the respective variable in each model grid cell with the corresponding cell thickness and summing to the depth where the lower edge of the grid cell is nearest to 200 m. We choose a depth of 200 m for the integration after examining the subseasonal anomalies (obtained as described in the preceding paragraph) of the ECCO potential temperature (see Movie S1), from which it is observed that the largest subseasonal anomalies of ocean temperature are between 50–150 m depths with maximum amplitude (>0.5°C) between 90–110 m depths. As such, a 200 m integration would sufficiently capture the strongest signal of S2S temperature anomalies, and OHC, in the upper ocean. The magnitude of the residual (left hand side minus right

hand side of Equation 1) is much smaller than the magnitude of the heat budget terms (not shown), and therefore the heat budget is essentially closed.

### 2.4. Balance Metric and Covariance Ratio

To better understand the contribution of multiple physical processes, we use a tracer Balance Metric, $M_B$ (Halkides et al., 2015). $M_B$ describes the balance of two processes, $P_1$ and $P_2$, relative to the tendency, $T_t$ on a certain timescale and at each location. $M_B$ can have a value between $-1$ and 1 and is defined as follows:

$$M_B(P_1, P_2) \equiv \frac{\langle (P_2 - T_t)^2 \rangle - \langle (P_1 - T_t)^2 \rangle}{\langle (P_2 - T_t)^2 \rangle + \langle (P_1 - T_t)^2 \rangle} \tag{2}$$

The terms in angled brackets represent the mean squared errors between $T_t$ and $P_1$ or $P_2$. If $M_B$ has a positive value at a given location, then the errors of process $P_1$ relative to the tracer tendency $T_t$ are smaller compared to process $P_2$. The more positive the value, the smaller the mean squared error of the process $P_1$ relative to $T_t$. Conversely, if $M_B$ has a negative value at a given location, then the errors of process $P_2$ relative to $T_t$ are smaller compared to process $P_1$. If $M_B$ is zero, both processes have comparable mean squared errors relative to $T_t$. In our case, $T_t$ is OHCT while $P_1$ and $P_2$ can be pairs of processes in the heat budget such as ADV and $Q$. One caveat when using the balance metric is that $M_B$ cannot directly tell us which process is driving $T_t$, since a process may have a small residual relative to $T_t$ but be anti-correlated with it. However, $M_B$ can be a useful metric to isolate the relative importance of two processes with similar amplitude that are correlated with $T_t$. Hence the balance metric spatial map is a good supplement to correlation spatial maps of physical processes in the heat budget.

To quantify the fractional variance each anomalous process can explain of the anomalous OHCT, we present the covariance ratio, $r_x$ (Tesdal & Abernathey, 2021). The covariance ratio is defined as follows:

$$r_x = \frac{\sigma(x,y)}{\sigma(y)^2} \tag{3}$$

where $\sigma(x,y)$ is the covariance between $x$ and $y$, and $\sigma(y)^2$ is the variance of $y$. In the context of our analysis, $x$ is a term in the heat budget and $y$ is the OHCT.

For a closed heat budget, that is, where the sum of the heat budget terms is exactly equal to the OHCT, the sum of the covariance ratios for the heat budget terms must be equal to one.

## 3. Results

### 3.1. Physical Processes Driving S2S OHC Variability

To identify the physical processes driving and damping subseasonal variability in OHCT, each anomalous heat budget term from Equation 1 is correlated with the anomalous OHCT (Figure 2). A positive correlation of a budget term with OHCT indicates that the budget term acts to drive the OHC changes, and negative correlations indicate that the budget term damps the changes (e.g., Buckley et al., 2014). While correlations do not imply causation, we rely on the fact that each process is obtained from a heat budget which is closed. Hence, we know that these are indeed processes contributing to changes in OHCT. As correlation provides no information on the relative strength of the terms in driving and damping OHCT variability, we also compute the spatial patterns of regressions between budget terms and OHCT. These are very similar to spatial patterns of correlations (not shown). Correlations between heat budget terms and OHC were also computed (not shown), with the relationships being consistent with OHC lagging OHCT. Hence, we choose to show spatial relationships with correlations between heat budget terms and OHCT. However, care must be taken when interpreting correlations between each budget term and OHCT, since the terms in the heat budget are not linearly independent.

Zonal advection (ADV$_x$) (Figure 2a) is highly correlated with OHCT along the equator, while meridional advection (ADV$_y$) (Figure 2b) begins to dominate poleward of 4° latitude in both hemispheres. Within 2–4° on either side of the equator, both zonal and meridional advection have similar positive correlations with OHCT, suggesting both zonal and meridional advection play important roles in driving OHCT variations in this narrow latitudinal band. Zonal advection is also important in driving OHCT south of the equator with positive
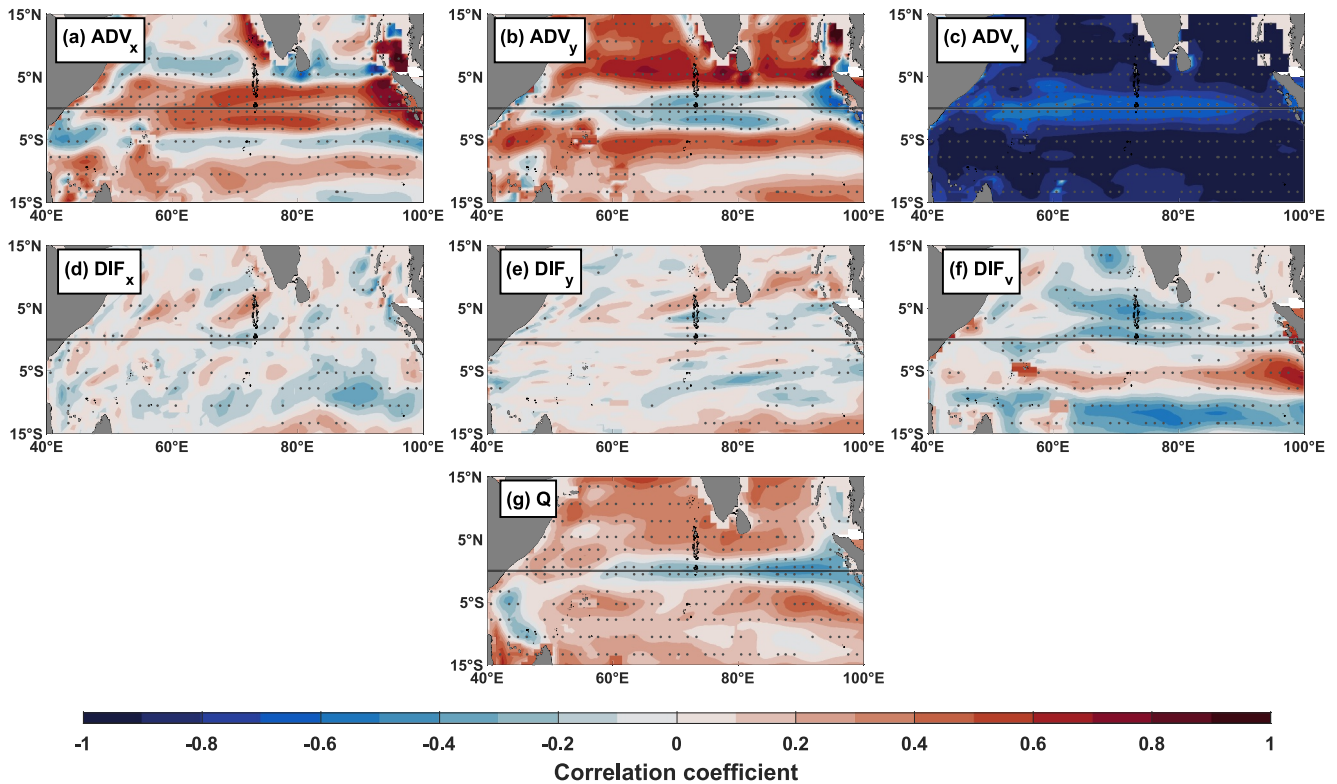
**Figure 2.** Correlations of 30–150 days bandpass filtered ocean heat content tendency with (a) zonal advection (b) meridional advection (c) vertical advection (d) zonal diffusion (e) meridional diffusion (f) vertical diffusion and (g) net air-sea heat fluxes. Stipples show regions where the correlations are statistically significant ($p < 0.05$) after considering serial correlation.

correlations between latitudes of approximately 12°S–8°S (Figure 2a). Vertical advection ($ADV_v$) (Figure 2c) is negatively correlated to OHCT, opposing the OHCT, therefore weakening or damping the OHC variations throughout the basin. Horizontal diffusion terms ($DIF_x$ and $DIF_y$) (Figures 2d and 2e) are weakly correlated with OHCT and have no discernible regular structure. Vertical diffusion ($DIF_v$) is positively correlated with OHCT south of the equator on the eastern part of the basin between 0 and 10°S and 80–100°E. The role of net air-sea heat flux ($Q$) is seen to become more important in contributing to driving OHCT as we move away from the equator, as seen from its positive correlation with OHCT (Figure 2g).

The covariance ratio is a useful metric to examine the fractional contribution of each heat budget term to the variance of OHCT (Figure 3). We supplement the covariance ratio with selected regional means of covariance ratios of advective processes on the model grid (Table 1), which differs slightly from the conventional zonal and meridional directions depicted in Figures 3a and 3b. This is because we use the model grid orientation to compute the covariance ratios of advective processes to ensure budget closure. We find that along the equator, zonal advection has the largest contribution to the variance of OHCT, with a mean covariance ratio of 2.67, while meridional advection contributes negatively with a mean covariance ratio of −0.95 as depicted in Figures 3a and 3b and Table 1. The large contribution of anomalous zonal advection to the correlation and covariance ratio south of the equator between 12°S and 8°S, as seen in Figures 2a and 3a, is likely associated with the Indonesian Throughflow (ITF). Contributions from non-advective processes such as net air-sea heat fluxes and diffusion are not shown as they are negligible. In the off-equatorial sections both north and south of the equator, we find that meridional advection has a larger contribution to the variance of OHCT with a mean covariance ratio of 1.62 in the northern section and 1.83 in the southern section Figure 3b. Vertical advection has mean covariance ratio that varies from around −0.7 to −0.9, and is about 50% of the magnitude of the covariance ratio of the horizontal advection terms, but of opposite sign. This is consistent with the vertical advection being the principal process damping subseasonal variability of OHC. Diffusion and net air-sea heat fluxes have a negligible contribution to the variance of OHCT. The sum of the covariance ratios of advective processes is approximately equal to one (Table 1), indicating that advective processes account for almost all the variance in OHCT.
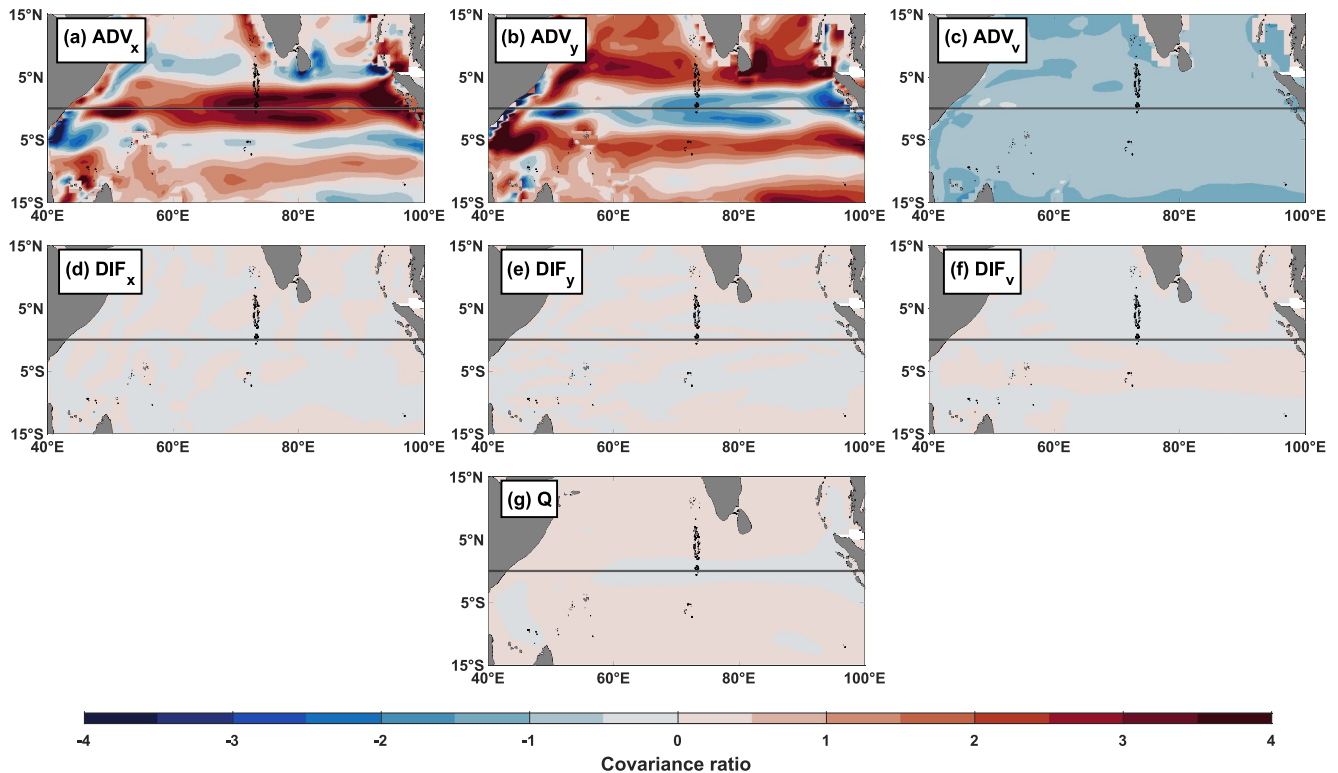
**Figure 3.** Covariance ratio of 30–150 days bandpass filtered ocean heat content tendency with (a) zonal advection (b) meridional advection (c) vertical advection (d) zonal diffusion (e) meridional diffusion (f) vertical diffusion and (g) net air-sea heat fluxes.

While correlations can show which processes are important in driving or damping OHCT, they provide no information on the amplitude of the terms. Therefore, in Supporting Information S1, we include figures of standard deviations of each heat budget term (Figure S1 in Supporting Information S1) as well as the root-mean-square error (RMSE) of each heat budget term with the OHCT (Figure S2 in Supporting Information S1) to give an indication of magnitudes and to quantify the deviation of each heat budget term from the OHCT.

To better understand the relative importance of pairs of processes, we show spatial maps of the Balance Metric, $M_B$ (Figure 4). We first compare the two physical processes that have the highest correlations, anomalous advection (ADV) and anomalous net air-sea heat flux ($Q$) (Figure 4a). The values close to −1 throughout the basin shows the dominance of advective processes over the surface fluxes. It is consistent with the advective processes explaining essentially all the OHC subseasonal variability (Table 1). Further, in Figure 4b, the positive values throughout the basin suggest that anomalous horizontal advection ($ADV_h$) contributes largely to the lower mean squared errors in the ADV term. A value of 0.6 as found over large regions of the Indian Ocean indicates that the squared difference of $ADV_h$ and OHCT is four times smaller than that of $ADV_v$ and OHCT, which is consistent with $ADV_v$ damping the OHC variability on subseasonal timescales (Figures 2 and 3 and Table 1).

**Table 1**
*Mean Covariance Ratio Explained by Model Grid Advective Processes in the North Section (Latitudes 3°N–5°N), Equatorial Section (Latitudes 2°S–2°N), and South Section (Latitudes 5°S–3°S)*

|  | Model $x$ component of advection | Model $y$ component of advection | Model vertical component of advection | Covariance ratio explained by the sum of advective processes |
|---|---|---|---|---|
| North section | 0.26 | 1.62 | −0.90 | 0.98 |
| Equatorial section | 2.67 | −0.95 | −0.71 | 1.01 |
| South section | −0.01 | 1.83 | −0.83 | 0.99 |

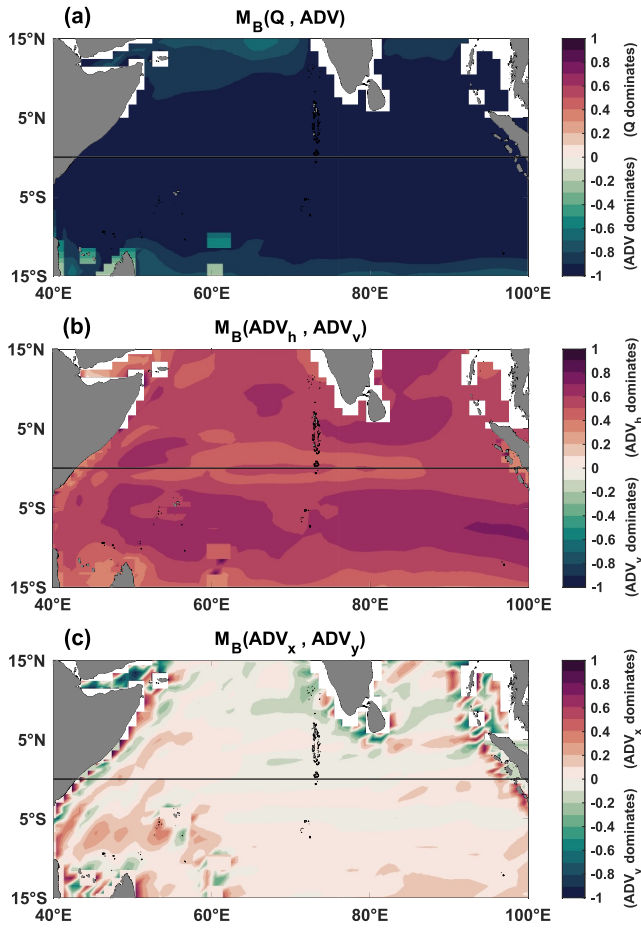*Note.* The longitudes used for averaging in all sections are 50°E–90°E.

**Figure 4.** Balance metric as defined in Halkides et al. (2015) for anomalous (a) net air-sea heat fluxes and three-dimensional advection, (b) horizontal advection and vertical advection and (c) zonal advection and meridional advection.

We compute the $M_B$ for anomalous $ADV_x$ and anomalous $ADV_y$ to see which component of horizontal advection dominates (Figure 4c). The $M_B$ for $ADV_x$ and $ADV_y$ shows values near zero, nevertheless the differences along the eastern and western boundaries indicate that anomalous $ADV_x$ contributes to the lower mean squared errors of anomalous $ADV_h$ along the boundaries. Along the west coast of India, anomalous $ADV_y$ becomes more important. The near zero values along the narrow equatorial band show that both $ADV_x$ and $ADV_y$ contribute nearly equally to lower values of mean squared errors in the upper 200 m of the Indian Ocean on S2S timescales (Figure 4c).

## 3.2. OHC and Physical Processes Associated With the MJO

Phase composites are computed to understand and quantify how the MJO impacts the upper OHC. We present the first four phases of the MJO when it is convectively enhanced over the Indian Ocean region (Figure 5). The MJO phase composites for phases 5 to 8 have similar patterns but with opposite signs as those patterns during phases 1 to 4 (see Figure S3 in Supporting Information S1). The MJO phase composites are made by averaging the filtered fields for the days that the MJO is in a particular phase and where the amplitude of the RMM indices exceeds 1. The composite averages are limited to the boreal winter (November–April) season when the MJO is known to dominate the S2S variability (Lau et al., 2012; Zhang, 2005). While the MJO explains relatively little variance in subseasonal OHC, the amplitude of the OHC associated with the MJO is substantial, being between 30% and 50% of the standard deviation of subseasonal OHC over large parts of the Indian Ocean (not shown).

The anomalous 5 m depth Potential Temperature $\theta$ (−5 m) from the ECCO data set is plotted to show the effect of the MJO on the ocean surface temperature (Figure 5, left panel). The $\theta$ (−5 m) patterns are largely like the SST patterns (see Sup Figures 4 and 5 for comparison with observed anomalous SST and OHC in the upper 100 m) and hence $\theta$ (−5 m) is interpreted as SST. Blue contours superimposed on $\theta$ (−5 m) are anomalous net air-sea heat fluxes with positive values downward, into the ocean. During the convectively enhanced phases of the MJO over the Indian Ocean, the anomalous net surface heat fluxes are negative and upward into the atmosphere over the Indian Ocean contributing to SST cooling. This is consistent with surface heat fluxes largely responsible for driving SST and MLT responses associated with the MJO with a 1 to 2 phase (approximately 6–12 days) delay.

The right panel in Figure 5 shows the anomalous OHC integrated within the upper 200 m in shading with anomalous OLR as contours. The anomalous OLR is used as a proxy for the large-scale convection associated with the MJO. The arrows show the anomalous adjusted zonal and meridional wind stress vectors. An eastward propagation of the MJO is seen in the anomalous OLR while the anomalous wind stress is easterly to the east of the convection and westerly to the west of the convection, typical of what is observed during the MJO. While SST shows anomalous cooling during the convectively enhanced phases of the MJO over the Indian Ocean, the OHC is anomalously high. This indicates that ocean dynamics are the dominant driver of OHC variations, rather than surface heat fluxes. This is consistent with Rydbeck et al. (2019), who first reported this anomalously warm OHC response during the convectively enhanced phases of the Intraseasonal Oscillation (ISO), which includes the MJO. Using HYCOM reanalysis, Rydbeck et al. (2019) looked at the integrated temperature up to the depth of the 26°C isotherm. We see similar patterns reproduced in anomalous OHC with our integration to a deeper depth (200 m) than the 26°C isotherm depth (40–85 m; Rydbeck et al. (2023)) used by Rydbeck et al. (2019).

The patterns in anomalous OHC variations along the equator (Figure 5) suggest that ocean dynamics play a role in contributing to these patterns. We further examine this by plotting three longitude-depth sections of anomalous potential temperature averaged between 3° and 5°N, 2°S and 2°N, and 5° and 3°S for different MJO phases (Figure 6). Along the equator the temperature anomalies are seen to propagate eastward (Figure 6b), consistent
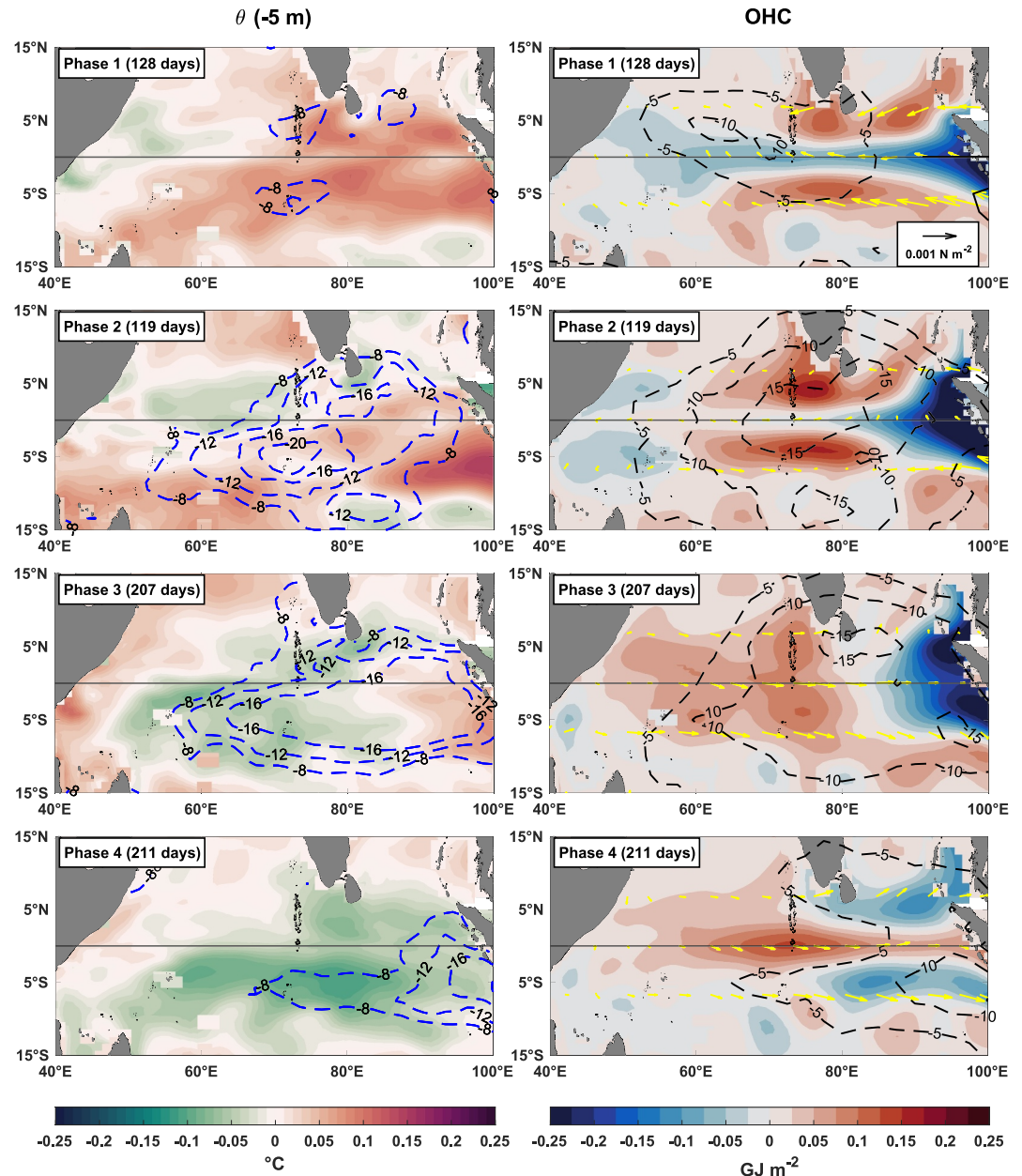
**Figure 5.** Composites of 30–150 days bandpass filtered (left) Potential Temperature at 5 m depth (shading, °C), net air-sea heat fluxes (blue contours, W m$^{-2}$; positive downwards) and (right) Ocean Heat Content integrated in the upper 200 m (shading, GJ m$^{-2}$), OLR (black contours, W m$^{-2}$) and adjusted horizontal surface wind stress (yellow arrows, N m$^{-2}$) during phases 1 to 4 of the MJO and for the November–April season. Dashed contours are negative anomalies while solid contours are positive anomalies for both net air-sea heat fluxes and OLR.

with Kelvin waves. The strongest temperature anomalies (>0.5°C) are observed below the mixed layer (black contour) and between depths of 50–150 m. Positive temperature anomalies are generated along the equator during Phase 2, largely due to a contribution from the westerly wind stress forcing associated with the active phase of the MJO (Figure 5). The positive subsurface ocean temperature anomalies are largely the result of the westerly wind stress forcing of downwelling Kelvin waves during the convective onset of the MJO which contributes to deepening isotherms such that warmer anomalies appear at deeper levels. These positive anomalies reach the eastern boundary by Phase 5, after which they are reflected and begin to propagate westward, consistent with Rossby waves (Figures 6a–6c).
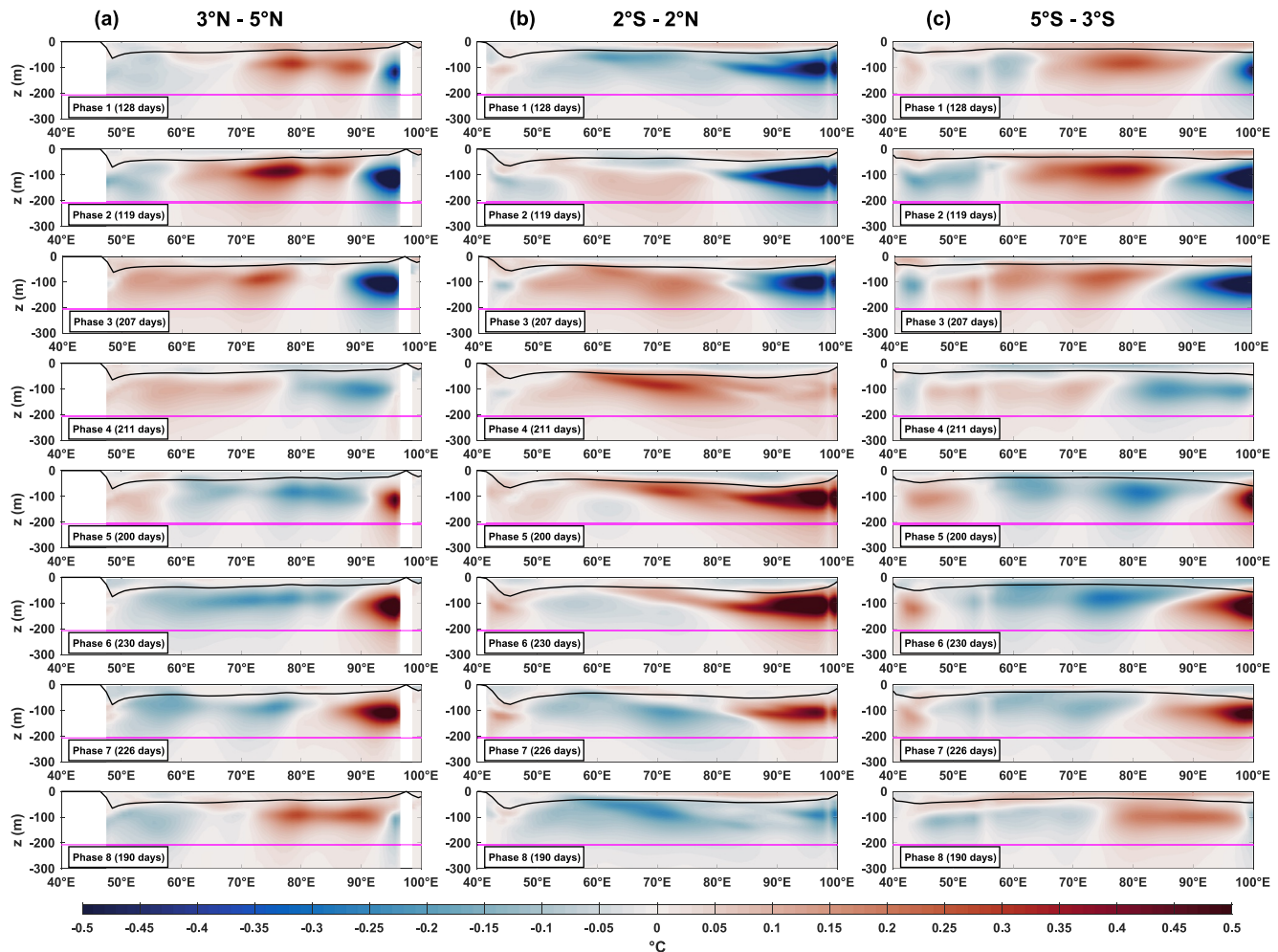
**Figure 6.** Composites of 30–150 days bandpass filtered ECCO potential temperature anomalies where each column shows the latitudinal averaged values in the (a) north off-equatorial section (3°–5°N), (b) equatorial section (2°S–2°N) and (c) south off-equatorial section (5°–3°S). The black solid contour is the mean mixed layer depth (not filtered) in each phase while the magenta line shows the depth to which integration is performed to obtain vertically integrated ocean heat content and heat budget terms. The mixed layer depth is defined as the depth where the potential density exceeds a variable threshold criterion which is equivalent to a decrease in temperature of 0.8°C (Kara et al., 2000).

These temperature anomalies suggest that equatorial wave dynamics are an important contributor to the evolution of OHC during the MJO (Figure 6). The maximum amplitude of these anomalies are below the mean mixed layer (depicted as the black contour), which is where the maximum anomalies associated with equatorial waves from low-order baroclinic modes would be seen. While the temperature response is largely consistent with processes driven by Kelvin waves along the equator and Rossby waves in the off-equatorial section, this cannot be explicitly confirmed without doing more sophisticated analysis, such as those used by Pujiana and McPhaden (2020) and Rydbeck et al. (2021) to isolate Kelvin waves and Rossby waves, respectively; this is beyond the scope of this study. Here, we are interested in variability on S2S timescales and not in the specific decomposition and effect of equatorial waves.

The phase-evolution of anomalous OHC and anomalous dynamic sea surface height associated with the MJO is depicted to better visualize the Kelvin and Rossby waves (Figure 7). The model state estimate compares well with the observed sea level anomalies from satellite altimetry (Figure S6 in Supporting Information S1). Along the equator, both the anomalous OHC and sea surface height are seen to propagate eastward with the evolution of the MJO, consistent with Kelvin waves while along the off-equatorial section, both OHC and sea surface height anomalies are observed to propagate westward, consistent with Rossby waves. This provides further support for the impact of equatorial waves on the OHC associated with the MJO.
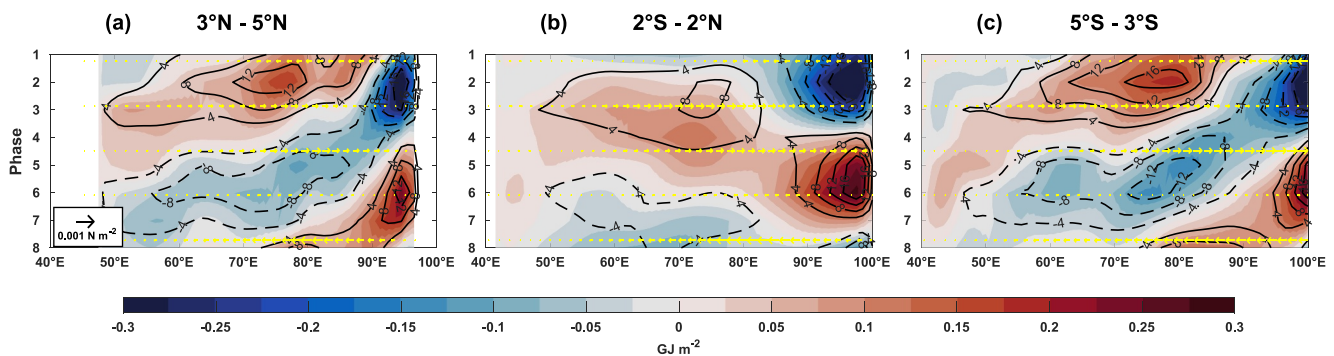
**Figure 7.** MJO Phase composites of 30–150 days bandpass filtered anomalous Ocean Heat Content (shading, GJ m$^{-2}$), anomalous model sea surface height corrected for the inverted barometer effect (contours, mm) and anomalous adjusted zonal wind stress (arrows, N m$^{-2}$) averaged between (a) 3°–5°N, (b) 2°S–2°N and (c) 5°–3°S. The anomalous sea surface height contours are in intervals of 4 mm. Dashed contours denote negative values, solid contours denote positive values, and the zero contour is omitted.

To examine the contribution of the physical processes driving subseasonal OHC variability associated with the MJO, longitude-phase vertically integrated (upper 200 m) anomalous heat budget terms are shown along three latitudinally averaged sections (Figure 8). Along the equator, zonal and meridional advection are in approximate balance and their sum determines the sign of OHCT (Figure 8b and Figure S7b in Supporting Information S1). On the eastern part of the basin, zonal advection has an amplitude an order of magnitude larger than OHCT with the same anomalous sign as OHCT in the region suggesting that it is the most important driver of OHC variability. Vertical advection, having an opposite anomalous sign (with magnitudes of 200–300 W m$^{-2}$) to OHCT along the equator, suggests that it is a process that has a damping effect on OHC variability. Additionally, vertical advection has magnitudes smaller than the horizontal advection terms, suggesting that horizontal advection is largely driving OHC variations associated with the MJO (see Figure S7 in Supporting Information S1 for the contribution of horizontal advection). Diffusion is seen to have a negligible effect on OHC variability. Net air-sea heat fluxes, having opposite anomalous sign (with magnitudes of 17–24 W m$^{-2}$) to OHCT, act to mainly damp OHC variations along the equator.

In the north off-equatorial section (Figure 8a), OHCT is largely dominated by meridional advection followed by zonal advection with a minor contribution from net air-sea heat fluxes. In the south off-equatorial section, OHCT is also dominated by meridional advection with minor contributions from net air-sea heat fluxes (Figure 8c). The amplitude of net air-sea heat fluxes are larger in the south off-equatorial section compared to the north and equatorial sections, but does not drive OHCT. Net air-sea heat fluxes are dominated by shortwave radiation (SW), followed by latent heat flux (LH) and sensible heat flux (SH) (see Figure S8 in Supporting Information S1). Anomalous longwave radiation (LW) provides a minor damping contribution to net air-sea heat flux.

## 4. Discussion and Conclusions

The physical processes governing changes of upper OHC on S2S timescales in the equatorial Indian Ocean have been investigated in a dynamically and kinematically consistent ocean state estimate. Horizontal advection was seen to be the most important driver of subseasonal OHC variations with zonal advection dominating along the equator and meridional advection dominating poleward of 5°. Along the equator, the approximate balance between anomalous zonal and meridional advection is the driver of anomalous OHCT. Vertical advection is important in damping the variability of OHCT off and along the equator. Halkides et al. (2015) found horizontal advection to be the dominant process along the equator in the mixed layer heat budget, while our results suggest that in addition to the mixed layer, horizontal advection is also the dominating process throughout the upper 200 m of the water column.

During the convectively enhanced phases of the MJO over the Indian Ocean, the SST response was consistent with net air-sea heat fluxes contributing to SST cooling while the OHC response over the western boundary and central Indian Ocean showed anomalous warming. The physical processes driving the observed variations of OHC associated with the MJO are found to be dominated by ocean dynamics as revealed by the importance of the advection term in the heat budget accounting for almost all the variance in OHCT. We find the largest S2S ocean
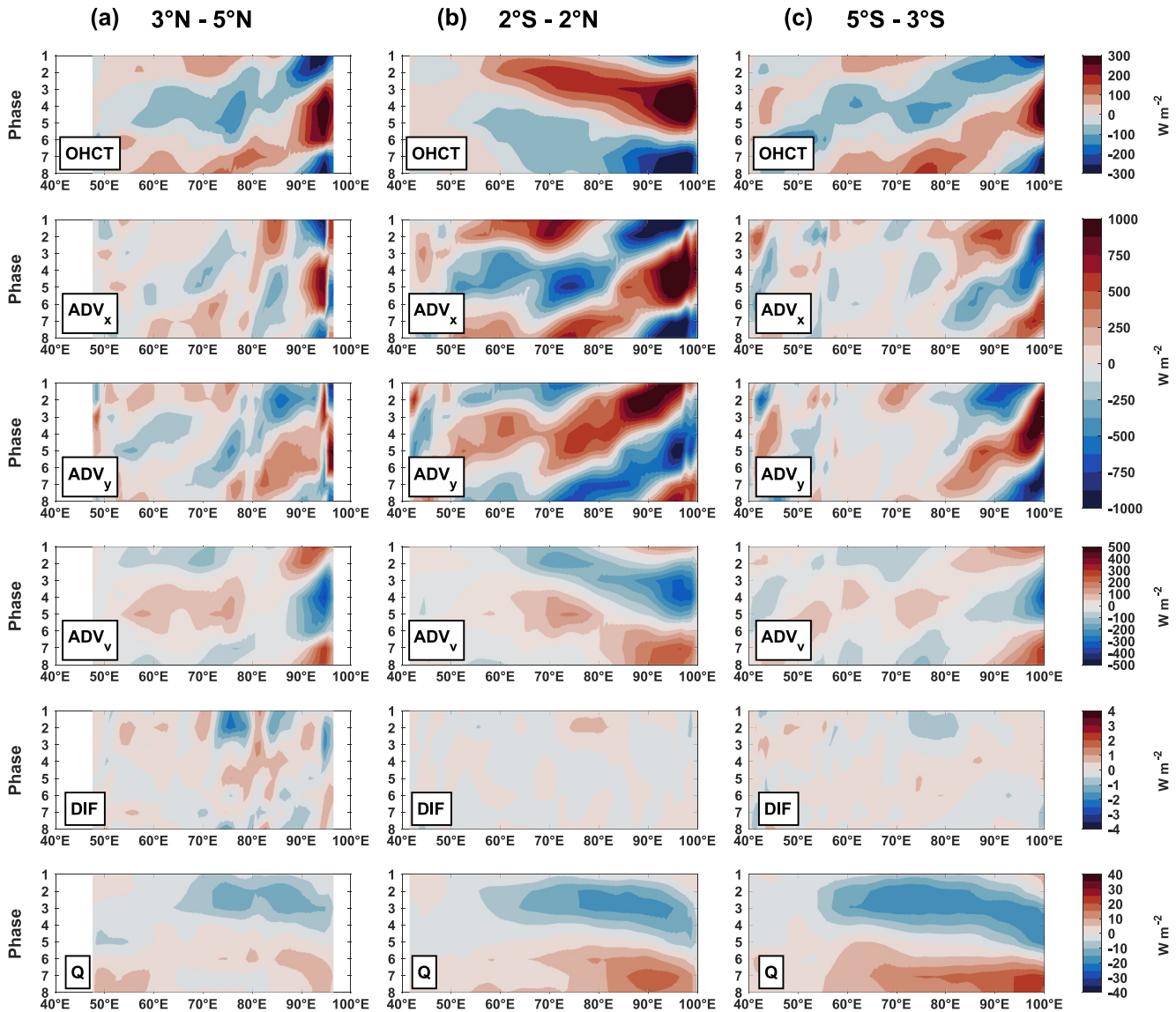
**Figure 8.** Hovmöller of anomalous heat budget terms (rows) during different MJO Phases averaged between (a) 3°–5°N, (b) 2°S–2°N and (c) 5°–3°S. OHCT, ADV$_x$, ADV$_y$, ADV$_v$, DIF, and $Q$ represent the ocean heat content tendency, zonal advection, meridional advection, vertical advection, diffusion, and net air-sea heat flux terms, respectively integrated within the upper 200 m.

temperature anomalies between depths of 50–150 m, as was also observed by Konda et al. (2023) during the Boreal Summer Intraseasonal Oscillation (BSISO).

Along both the equatorial and off-equatorial sections, horizontal advection drives OHC variations. In connection with the advective processes, equatorial waves are seen to be important in driving OHC variations. The eastward propagating patterns of anomalous OHC along the equator are consistent with processes driven by Kelvin waves while the westward propagating patterns of OHC slightly off the equator are consistent with processes driven by Rossby waves (Figure 7). It should be noted that the MJO can also drive Wyrtki jets, which can contribute to zonal advection (e.g., McPhaden & Foltz, 2013). The Wyrtki jets have a strong seasonal dependence typically being more pronounced during fall and spring while the Equatorial Undercurrent is more evident when the winds have an easterly component from February to June (Prerna et al., 2019; Schott et al., 2009; Wyrtki, 1973). As such, removing the seasonal cycle and limiting the composites to just the boreal winter season minimizes the contribution of Wyrtki jets and the Equatorial Undercurrent to zonal advection, but it does not completely remove it. While previous studies have identified subseasonal variability in the Wyrtki jet with peaks in spring and fall (e.g.,

Prerna et al., 2019), investigating the impact of the Wyrtki jet on subseasonal OHC variability is beyond the scope of this paper.

We do note that while horizontal advection is the most important driver of subseasonal OHC variations, it is also a process with large uncertainties that are difficult to quantify. Subsurface ocean currents are less constrained in ECCO compared to ocean temperature, largely due to fewer subsurface observations of ocean currents. Better constraining ocean currents necessitates more subsurface current observations, which in future ocean state estimates can contribute to reducing uncertainties in advective processes.

We find OHC patterns associated with the MJO to be similar to those in Rydbeck et al. (2019). Our heat budget analysis is integrated to a deeper depth (200 m; below the mixed layer) compared to the 26°C isotherm depth (40–85 m) used by Rydbeck et al. (2019). Integration to different depths can lead to different interpretations of the OHC patterns, although they may look similar. We find the largest temperature anomalies propagating zonally below the mixed layer (Figure 6 and Movie S1). While vertical advection of heat is an important term in the heat budget for the mixed layer and the layers below, horizontal advection becomes more important when integrating over multiple layers.

Our heat budget analysis reveals horizontal advection as the dominant driver of subseasonal OHC variability. This study extends on some of the work of Rydbeck et al. (2021), which used a Rossby wave index to only look at OHC variations associated with ocean dynamics. A limitation of performing heat budget analysis using ocean reanalysis products constrained using data assimilation, such as those from HYCOM used by Rydbeck et al. (2021), is that these ocean reanalysis products do not have budget closure due to data assimilation creating analysis increments. Ocean state estimates, such as ECCO used in our study, do not have this limitation as the model conservation laws are satisfied such that each physical process is known and can be accurately quantified. Physical processes driving OHC variability on these timescales have not previously been quantified in a dynamically and kinematically consistent manner using ocean state estimates, and this is an important contribution of this study.

Our heat budget analysis adds further support that subseasonal OHC in the equatorial Indian Ocean is largely driven by ocean dynamics with net air-sea heat fluxes playing a minor role. In addition, we find that positive OHC anomalies modulated by Rossby waves (partly a result of reflected downwelling Kelvin waves) reach the central Indian Ocean as the MJO intensifies in phases 2 and 3 (Figures 7a–7c). These results are consistent with the synchronization between ocean dynamics (seen from sea level anomalies) and the MJO. The synchronization between OHC modulated by ocean dynamics and intraseasonal variability supports previous studies for example (Rydbeck et al., 2021; Webber et al., 2010, 2012), and suggests that ocean dynamics may be an important component of the MJO.

## Data Availability Statement

The ECCO Version 4 Release 4 Dataset (Wang & Fenty, 2021) including the daily ocean currents, temperature, mixed layer depth, adjusted surface forcing fields, and model diagnostics used for the heat budget analysis developed by the ECCO Consortium, Fukumori, I., Wang, O., Fenty, I., Forget, G., Heimbach, P., and Ponte, R. M. was retrieved from https://data.nas.nasa.gov/ecco/data.php?dir=/eccodata/llc_90/ECCOv4/Release4.

NOAA Interpolated Outgoing Longwave Radiation (OLR) data (Liebmann & Smith, 2021) was provided by the NOAA PSL, Boulder, Colorado, USA, from their website at https://psl.noaa.gov/data/gridded/data.olrcdr.interp.html. The RMM indices, MJO amplitude and phase data (Wheeler & Hendon, 2021) was provided by the Australian Bureau of Meteorology and can be obtained from their website at http://www.bom.gov.au/climate/mjo/.

The satellite altimeter sea level anomaly (SLA) data (CMEMS, 2023) was obtained from the E.U. Copernicus Marine Service Information; https://doi.org/10.48670/moi-00148.

NOAA OI SST V2 High Resolution Dataset (Huang et al., 2023) was provided by the NOAA PSL, Boulder, Colorado, USA, from their website at https://psl.noaa.gov/data/gridded/data.noaa.oisst.v2.highres.html.

The equatorial mooring data during the DYNAMO field campaign was obtained from the DYNAMO Legacy Collection (Lien & Moum, 2019) hosted by UCAR/NCAR - Earth Observing Laboratory on their website at https://data.eol.ucar.edu/dataset/347.230.

The MATLAB/Octave toolbox gcmfaces has been used to read and process the ECCOv4r4 files. The gcmfaces toolbox is available on GitHub (https://github.com/MITgcm/gcmfaces; Forget et al. (2020)).

The Climate Data Toolbox (CDT) for MATLAB (Greene, 2019) was used to remove the seasonal cycle and apply the bandpass filtering. The CDT is available on GitHub (https://github.com/chadagreene/CDT; Greene et al. (2019)).

A licensed version of MATLAB (MATLAB R2020b) was used for analysis and figure generation.

# References

Boulanger, J. P., & Menkes, C. (1995). Propagation and reflection of long equatorial waves in the Pacific Ocean during the 1992-1993 El Nino. *Journal of Geophysical Research*, *100*(C12), 25041–25059. https://doi.org/10.1029/95jc02956

Buckley, M. W., Ponte, R. M., Forget, G., & Heimbach, P. (2014). Low-frequency SST and upper-ocean heat content variability in the North Atlantic. *Journal of Climate*, *27*(13), 4996–5018. https://doi.org/10.1175/jcli-d-13-00316.1

Cane, M. A., & Moore, D. W. (1981). A note on low-frequency equatorial basin modes. *Journal of Physical Oceanography*, *11*, 1578–1584. https://doi.org/10.1175/1520-0485(1981)011<1578:anolfe>2.0.co;2

Cane, M. A., & Sarachik, E. S. (1977). Forced baroclinic ocean motions: II. The linear equatorial bounded case. *Journal of Marine Research*, *35*.

Chi, N. H., Lien, R. C., D'Asaro, E. A., & Ma, B. B. (2014). The surface mixed layer heat budget from mooring observations in the central Indian Ocean during Madden-Julian Oscillation events. *J Geophys Res-Oceans*, *119*(7), 4638–4652. https://doi.org/10.1002/2014jc010192

CMEMS. (2023). Global ocean gridded L 4 sea surface heights and derived variables reprocessed 1993 ongoing (Version vDec2021) [Dataset]. Copernicus Marine Environment Monitoring Service. https://doi.org/10.48670/moi-00148

Dee, D. P., Uppala, S. M., Simmons, A. J., Berrisford, P., Poli, P., Kobayashi, S., et al. (2011). The ERA-interim reanalysis: Configuration and performance of the data assimilation system. *The Quarterly Journal of the Royal Meteorological Society*, *137*(656), 553–597. https://doi.org/10.1002/qj.828

DeMott, C. A., Klingaman, N. P., & Woolnough, S. J. (2015). Atmosphere-ocean coupled processes in the Madden-Julian oscillation. *Reviews of Geophysics*, *53*(4), 1099–1154. https://doi.org/10.1002/2014rg000478

Drushka, K., Sprintall, J., Gille, S. T., & Wijffels, S. (2012). In situ observations of Madden-Julian oscillation mixed layer dynamics in the Indian and Western Pacific Oceans. *Journal of Climate*, *25*(7), 2306–2328. https://doi.org/10.1175/jcli-d-11-00203.1

Ducet, N., Le Traon, P. Y., & Reverdin, G. (2000). Global high-resolution mapping of ocean circulation from TOPEX/Poseidon and ERS-1 and-2. *Journal of Geophysical Research*, *105*(C8), 19477–19498. https://doi.org/10.1029/2000jc900063

ECCO Consortium, F. I., Wang, O., Fenty, I., Forget, G., Heimbach, P., & Ponte, R. M. (2021). Synopsis of the ECCO central production global ocean and sea-ice state estimate (Version 4 Release 4).

Forget, G., Campin, J. M., Heimbach, P., Hill, C. N., Ponte, R. M., & Wunsch, C. (2015). ECCO version 4: An integrated framework for non-linear inverse modeling and global ocean state estimation. *Geoscientific Model Development*, *8*(10), 3071–3104. https://doi.org/10.5194/gmd-8-3071-2015

Forget, G., Milechin, L., & Owang (2020). gaelforget/gcmfaces: Update `read_nctiles` + various Lagrangian, vorticity, and divergence tools (Version v1.5.0) [Software]. Zenodo. https://doi.org/10.5281/zenodo.3606908

Gaspar, P., Gregoris, Y., & Lefevre, J. M. (1990). A simple eddy kinetic-energy model for simulations of the oceanic vertical mixing - Tests at station papa and long-term upper ocean study site. *Journal of Geophysical Research*, *95*(C9), 16179–16193. https://doi.org/10.1029/jc095ic09p16179

Greene, C. A. (2019). The climate data toolbox for MATLAB. (Version 1.01) [Software]. GitHub. https://github.com/chadagreene/CDT

Greene, C. A., Thirumalai, K., Kearney, K. A., Delgado, J. M., Schwanghart, W., Wolfenbarger, N. S., et al. (2019). The climate data toolbox for MATLAB. *Geochemistry, Geophysics, Geosystems*, *20*(7), 3774–3781. https://doi.org/10.1029/2019gc008392

Halkides, D. J., Waliser, D. E., Lee, T., Menemenlis, D., & Guan, B. (2015). Quantifying the processes controlling intraseasonal mixed-layer temperature variability in the tropical Indian Ocean. *Journal of Geophysical Research: Oceans*, *120*(2), 692–715. https://doi.org/10.1002/2014jc010139

Heimbach, P., Hill, C., & Giering, R. (2005). An efficient exact adjoint of the parallel MIT General Circulation Model, generated via automatic differentiation. *Future Generation Computer Systems*, *21*(8), 1356–1371. https://doi.org/10.1016/j.future.2004.11.010

Hendon, H. H., Liebmann, B., & Glick, J. D. (1998). Oceanic Kelvin waves and the Madden-Julian oscillation. *Journal of the Atmospheric Sciences*, *55*(1), 88–101. https://doi.org/10.1175/1520-0469(1998)055<0088:okwatm>2.0.co;2

Huang, B. Y., Liu, C., Banzon, V., Freeman, E., Graham, G., Hankins, B., et al. (2021). Improvements of the daily optimum interpolation sea surface temperature (DOISST) version 2.1. *Journal of Climate*, *34*(8), 2923–2939. https://doi.org/10.1175/jcli-d-20-0166.1

Huang, B. Y., Liu, C. Y., Banzon, V., Freeman, E., Graham, G., Hankins, B., et al. (2023). NOAA OI SST V2 high resolution dataset [Dataset]. NOAA PSL. https://psl.noaa.gov/data/gridded/data.noaa.oisst.v2.highres.html

IOC, S. (2010). IAPSO: The international thermodynamic equation of seawater–2010: Calculation and use of thermodynamic properties, Intergovernmental Oceanographic Commission, manuals and guides No. 56. *UNESCO, Manuals and Guides*, *56*, 1–196.

Kara, A. B., Rochford, P. A., & Hurlburt, H. E. (2000). An optimal definition for ocean mixed layer depth. *Journal of Geophysical Research*, *105*(C7), 16803–16821. https://doi.org/10.1029/2000jc900072

Konda, G., Gulakaram, V. S., & Vissa, N. K. (2023). Intraseasonal variability of subsurface ocean temperature anomalies in the Indian Ocean during the summer monsoon season. *Ocean Dynamics*, *73*(3–4), 165–179. https://doi.org/10.1007/s10236-023-01547-x

Lau, W. K. M., Waliser, D. E., & Goswami, B. N. (2012). South Asian monsoon. In *Intraseasonal variability in the atmosphere-ocean climate system* (pp. 21–72). Springer Berlin Heidelberg.

Liebmann, B., & Smith, C. A. (1996). Description of a complete (interpolated) outgoing longwave radiation dataset. *Bulletin America Meteorology Social*, *77*, 1275–1277.

Liebmann, B., & Smith, C. A. (2021). NOAA interpolated outgoing longwave radiation (OLR) [Dataset]. NOAA PSL. https://psl.noaa.gov/data/gridded/data.olrcdr.interp.html

Lien, R., & Moum, J. (2019). DYNAMO sub-surface mooring data: DYNAMO legacy collection (version 1.0) [Dataset]. UCAR/NCAR - Earth Observing Laboratory. https://doi.org/10.26023/JTGJ-4JG4-AD0W

Marshall, J., Adcroft, A., Hill, C., Perelman, L., & Heisey, C. (1997). A finite-volume, incompressible Navier Stokes model for studies of the ocean on parallel computers. *Journal of Geophysical Research*, *102*(C3), 5753–5766. https://doi.org/10.1029/96jc02775

Matthews, A. J., Singhruck, P., & Heywood, K. J. (2010). Ocean temperature and salinity components of the Madden-Julian oscillation observed by Argo floats. *Climate Dynamics*, *35*(7–8), 1149–1168. https://doi.org/10.1007/s00382-009-0631-7

McDougall, T. J., & Barker, P. M. (2011). Getting started with TEOS-10 and the Gibbs seawater (GSW) oceanographic toolbox. *SCOR/IAPSO WG*, *127*, 1–28.

McPhaden, M. J., & Foltz, G. R. (2013). Intraseasonal variations in the surface layer heat balance of the central equatorial Indian Ocean: The importance of zonal advection and vertical mixing. *Geophysical Research Letters*, *40*(11), 2737–2741. https://doi.org/10.1002/grl.50536

Moum, J. N., Pujiana, K., Lien, R. C., & Smyth, W. D. (2016). Ocean feedback to pulses of the Madden-Julian Oscillation in the equatorial Indian Ocean. *Nature Communications*, *7*(1), 13203. https://doi.org/10.1038/ncomms13203

Pascual, A., Faugere, Y., Larnicol, G., & Le Traon, P. Y. (2006). Improved description of the ocean mesoscale variability by combining four satellite altimeters. *Geophysical Research Letters*, *33*(2), L02611. https://doi.org/10.1029/2005gl024633

Paulson, C. A., & Simpson, J. J. (1977). Irradiance measurements in the upper ocean. *Journal of Physical Oceanography*, *7*(6), 952–956. https://doi.org/10.1175/1520-0485(1977)007<0952:imituo>2.0.co;2

Piecuch, C. G. (2017). A note on practical evaluation of budgets in ECCO version 4 release 3.

Prerna, S., Chatterjee, A., Mukherjee, A., Ravichandran, M., & Shenoi, S. S. C. (2019). Wyrtki jets: Role of intraseasonal forcing. *Journal of Earth System Science*, *128*(1), 21. https://doi.org/10.1007/s12040-018-1042-0

Pujiana, K., & McPhaden, M. J. (2020). Intraseasonal kelvin waves in the equatorial Indian Ocean and their propagation into the Indonesian Seas. *Journal of Geophysical Research: Oceans*, *125*(5), e2019JC015839. https://doi.org/10.1029/2019jc015839

Redi, M. H. (1982). Oceanic isopycnal mixing by coordinate rotation. *Journal of Physical Oceanography*, *12*(10), 1154–1158. https://doi.org/10.1175/1520-0485(1982)012<1154:oimbcr>2.0.co;2

Reynolds, R. W., Smith, T. M., Liu, C., Chelton, D. B., Casey, K. S., & Schlax, M. G. (2007). Daily high-resolution-blended analyses for sea surface temperature. *Journal of Climate*, *20*(22), 5473–5496. https://doi.org/10.1175/2007jcli1824.1

Rydbeck, A. V., A Christophersen, J., Flatau, M. K., Janiga, M. A., Jensen, T. G., Reynolds, C. A., et al. (2023). Anchoring intraseasonal air-sea interactions: The moored moist static energy budget in the Indian Ocean from reanalysis. *Journal of Climate*, *36*(3), 959–981. https://doi.org/10.1175/jcli-d-22-0182.1

Rydbeck, A. V., Jensen, T. G., & Flatau, M. K. (2021). Reciprocity in the Indian Ocean: Intraseasonal oscillation and ocean planetary waves. *Journal of Geophysical Research: Oceans*, *126*(9), e2021JC017546. https://doi.org/10.1029/2021jc017546

Rydbeck, A. V., Jensen, T. G., & Nyadjro, E. S. (2017). Intraseasonal sea surface warming in the western Indian Ocean by oceanic equatorial Rossby waves. *Geophysical Research Letters*, *44*(9), 4224–4232. https://doi.org/10.1002/2017gl073331

Rydbeck, A. V., Jensen, T. G., Smith, T. A., Flatau, M. K., Janiga, M. A., Reynolds, C. A., & Ridout, J. A. (2019). Ocean heat content and the intraseasonal oscillation. *Geophysical Research Letters*, *46*(24), 14558–14566. https://doi.org/10.1029/2019gl084974

Schott, F. A., Xie, S. P., & McCreary, J. P. (2009). Indian Ocean circulation and climate variability. *Reviews of Geophysics*, *47*(1), RG1002. https://doi.org/10.1029/2007rg000245

Shinoda, T. (2005). Impact of the diurnal cycle of solar radiation on intraseasonal SST variability in the Western Equatorial Pacific. *Journal of Climate*, *18*(14), 2628–2636. https://doi.org/10.1175/jcli3432.1

Shinoda, T., Jensen, T. G., Flatau, M., & Chen, S. (2013). Surface wind and upper-ocean variability associated with the Madden–Julian Oscillation simulated by the coupled ocean–atmosphere mesoscale prediction system (COAMPS). *Monthly Weather Review*, *141*(7), 2290–2307. https://doi.org/10.1175/mwr-d-12-00273.1

Tesdal, J. E., & Abernathey, R. P. (2021). Drivers of Local Ocean heat content variability in ECCOv4. *Journal of Climate*, *34*(8), 2941–2956. https://doi.org/10.1175/jcli-d-20-0058.1

Wang, O., & Fenty, I. (2021). Estimating the circulation and climate of the ocean (ECCO) (Version 4, Release 4) [Dataset]. NASA. https://data.nas.nasa.gov/ecco/data.php?dir=/eccodata/llc_90/ECCOv4/Release4

Webber, B. G. M., Matthews, A. J., & Heywood, K. J. (2010). A dynamical ocean feedback mechanism for the Madden-Julian Oscillation. *The Quarterly Journal of the Royal Meteorological Society*, *136*(648), 740–754. https://doi.org/10.1002/qj.604

Webber, B. G. M., Matthews, A. J., Heywood, K. J., & Stevens, D. P. (2012). Ocean Rossby waves as a triggering mechanism for primary Madden-Julian events. *The Quarterly Journal of the Royal Meteorological Society*, *138*(663), 514–527. https://doi.org/10.1002/qj.936

Wheeler, M. C., & Hendon, H. H. (2004). An all-season real-time multivariate MJO index: Development of an index for monitoring and prediction. *Monthly Weather Review*, *132*(8), 1917–1932. https://doi.org/10.1175/1520-0493(2004)132<1917:aarmmi>2.0.co;2

Wheeler, M. C., & Hendon, H. H. (2021). RMM data [Dataset]. Bureau of Meteorology. http://www.bom.gov.au/climate/mjo/graphics/rmm.74toRealtime.txt

Wunsch, C., & Heimbach, P. (2013). Dynamically and kinematically consistent global ocean circulation and ice state estimates. In G. Siedler, S. M. Griffies, J. Gould, & J. A. Church (Eds.), *Ocean circulation and climate - A 21st century perspective* (pp. 553–579). Academic Press.

Wyrtki, K. (1973). An equatorial jet in the Indian Ocean. *Science*, *181*(4096), 262–264. https://doi.org/10.1126/science.181.4096.262

Zhang, C. (2005). Madden-Julian Oscillation. *Reviews of Geophysics*, *43*(2), RG2003. https://doi.org/10.1029/2004rg000158